Impact of free volume on shear band multiplication and bending plasticity

J. Li[a], C.H. Ke[b], X. Tong[a], Y.F. Jia[a], S.W. Wu[a], Y.D. Jia[a], J. Yi[a], G. Wang[a,*]

[a] Laboratory for Microstructures, Institute of Materials, Shanghai University, Shanghai 200444, China
[b] Department of Mechanical Engineering, State University of New York at Binghamton, Binghamton, NY 13902, USA

ARTICLE INFO

ABSTRACT

In-situ electron microscopy mechanical testing is a promising deformation observation technology that has been extensively applied to explore the deformation and fracture behaviour of MGs. In this paper, we adopt it in conjunction with digital image correlation technique to investigate the impact of free volume on shear band multiplication and bending plasticity in MGs. The strain evolutions of the notched Zr-, Ce- and Mg-based MGs are studied respectively. The results indicate that the strain-concentration striations before yielding contain amounts of free volume can improve the shear band multiplication, and are beneficial to the subsequent bending plasticity. Such conclusions successively verify a novel integrated method to explore the in-situ strain field evolution process near the notch of MGs, which is advantage for understanding the deformation and fracture behaviour of MGs in a complex stress state.

1. Introduction

Metallic glasses (MGs) with a disordered atomic structure usually exhibit unique and superior mechanical, physical and chemical properties [1–3], and hold promise for many engineering applications [4,5]. Unlike the dislocation motion in crystals, a frequently invoked concept in plastic deformation of MGs is a comparative process including the creating and annihilating processes of free volumes [6]. For in-homogeneous plastic flow at room temperature, the strain is localized in a few bands with increasing free volume, which results in overall softening, and the "soft" regions are origins for the nucleation of the shear bands [7,8]. Although MGs with different compositions usually have the same structure, i.e., glassy phase, they exhibit distinctly mechanical behaviors. In general, MGs with a high fracture toughness, such as Zr- and Cu-based MGs [9,10], are attributed to a significant crack tip plastic deformation [11], and have a limit plastic strain ability (compressively plastic strain value being less than 2%) [12]. However, some MGs, such as Mg- and La-based MGs [13,14], exhibit a low toughness, accompanied with little plastic strain. MGs with toughness values ranging from 2 to 86 MPa m$^{1/2}$ open a window to comparatively investigate the relationship between fracture toughness and fracture behaviour.

Digital image correlation (DIC) technique, as a strain analysis method, is a valuable technique to analyze the deformation behaviour and the fracture mechanism of MGs. It provides full-field displacements and strains by comparing the digital images of the specimen surface in the un-deformed (or reference) and deformed states respectively [15–18]. DIC has been employed to investigate the mechanical behaviour of MGs, such as residual stress distribution [19–22], shear band evolution and interaction [23–25], strain-energy transportation [26], etc. Moreover, the deformation evolution of MGs under bending is useful to understand the deformation behaviour of MGs because the sample is under a complex stress state, i.e., the sample resists both tensile and compressive stresses with gradient magnitudes [27–30].

In this paper, in-situ electron-microscopy mechanical testing techniques in conjunction with DIC technique is employed to investigate the strain-evolution process during three-point bending tests of notched MGs. Three MGs, i.e., $Zr_{52.5}Cu_{17.9}Ni_{14.6}Al_{10}Ti_5$ (at%), $Ce_{70}Ga_8Cu_{22}$ and $Mg_{65}Cu_{25}Gd_{10}$ with toughness values of 43, 6 and 2 MPa m$^{1/2}$ [26], are selected as the model materials, respectively. Then the corresponding quantitative analyses are carried out correspondingly. Finally, the failure modes and fracture process for the three model MGs are discussed in details.

2. Experimental procedure

The $Zr_{52.5}Cu_{17.9}Ni_{14.6}Al_{10}Ti_5$ (Zr-based) and $Ce_{70}Ga_8Cu_{22}$ (Ce-based) alloys were prepared by suction casting into Cu-mould to form rod-like MGs. The $Mg_{65}Cu_{25}Gd_{10}$ (Mg-based) MG was prepared by induction melting plus injection preparing rod samples. The diameters of three MGs were 3 mm. Compression specimens with the length of 6 mm were cut from the rod samples. The ends of each specimen were ground

Table 1
Summary of data on factors of activation barriers for shear flow or cavitation. B, G and T_g respectively represent elastic constant of bulk modulus, shear modulus and glass transportation temperature.

Sample	B (GPa)	G (GPa)	T_g (K)	$log(f)$
Zr-based MG	114.1 ± 6.9	32.3 ± 0.9	653 [35]	5.6
Ce-based MG	31.8 ± 3.8	11.4 ± 1.2	363 [36]	2.2
Mg-based MG	45.1 ± 4.6	19.3 ± 1.0	424 [37]	1.9

to a surface roughness of less than 1 μm. Compression tests were conducted using an MTS CMT5205 machine at room temperature and a strain rate of 1.5×10^{-4} s^{-1}. The MG specimens with sizes of $12 \times 2.5 \times 1.6$ mm^3 were cut from rod-like samples by using a diamond saw with water cooling, and a notch with a radius of 100 μm and a length of about 400 μm was cut in the middle of the sample by a diamond wire saw for three-point bending test. Then, the samples were carefully polished to remove surface marks to impart a smooth and flat surface. The amorphous nature of the MGs was identified by the X-ray diffraction (XRD) in a Rigaku DLMAX-2550 diffractometer with the Cu-K_α radiation (λ = 0.1542 nm). The bulk and shear modulus measured by an Olympus Panametrics NDT 5900PR ultrasonic testing device. The results are listed in Table 1. The strain field of the MGs' surfaces was visualized by interpreting the bending measurements using the DIC method. In this experiment, a copper grid with 2000 mesh (G2000HS-C3 from Gilder Grids Company) was put on the surface of the specimen, and covered the crack tip. Then, the specimen covered by the copper grid was deposited by a thin layer of Pt film with a thickness of 20 nm in a sputtering system. The mesh grid pattern was transferred onto the specimen surface, and the pitch size of the mesh was measured to be about 12.5 μm. Subsequently, the specimen was mounted in a loading cell (Gatan Microtest Series) for *in-situ* mechanical measurements inside a CamScan Apollo 300 type scanning electron microscope (SEM), as shown in Fig. 1. The SEM images were captured at a variety of loads during the three-point bending test. The loading rate was set as 0.5 mm/min. The size of SEM imagine was 1280×1024 $pixels^2$, and a length-pixel ratio was approximately 0.938 μm/pixel. A 720×540 $pixel^2$ (about 675×507 $μm^2$) domain, which was located near the notch of the sample, was adopted for DIC calculation. An un-deformed image was obtained prior to loading as a reference record. And a series of strain field distribution contour maps under different stresses could then be calculated by DIC software.

3. Results and discussion

Three MGs exhibit obviously different fracture behaviors upon compressing (Fig. 2). The Zr-based MG shows an elasto-plastic deformation behaviour with the largest compressive ductility in three

MGs. The Ce-based MG shows a slightly plastic deformation after yielding. The Mg-based MG displays elastic deformation without any plasticity before fracture. Representative normal stress and midpoint strain curves under three-point bending test for three types of MGs are plotted in Fig. 3. The normal stress, σ_{nom}, is generally obtained according to the Classic Beam Theory, and the midpoint strain, ε, can be calculated by the maximal midpoint deflections,

$$\sigma_{nom} = \frac{3PL_0}{2b(h - \alpha_0)^2}, \tag{1}$$

$$\varepsilon = \frac{6Bb}{L_0^2}, \tag{2}$$

where P is the applied force, L_0 is the spanning distance, b is the thickness, h is the width, α_0 is the length of the notch and B is the maximal deflection of the midpoint. The normal stress-midpoint strain curve of the Zr-based MG can be divided into two stages including an elastic deformation (linear portion) and a plastic deformation (nonlinear portion). It presents the largest bending ductility with a maximum normal stress of approximately 3455 MPa. However, the curves of the Ce- and Mg-based MGs are both linear, which indicate no plastic deformation before failure. Their corresponding stresses are measured and the values lie in about 215 and 56 MPa before failure, respectively. Due to there was no CCD conjunct with this scanning electron microscope, SEM images of the specimen was acquired *in-situ* after each step of loading. It took some time to capture the SEM. During that time, the loading cell would relax and the load (or the stress) would decrease to form the serration on the stress-strain curves [31].

Additionally, the crack-formation processes of three types of MGs are captured and visualized in the recoded SEM images to discover the different failure modes. For the Zr-based MG, four stages for the bending process can be captured and drawn in Fig. 4. In stage I [shown in Fig. 4(a) and (b)], the Zr-based MG appears an elastic deformation and no obvious shear bands appear on the side-view image. After the elastic stage, the Zr-based MG displays some local plastic deformation, and some shear bands emerge around the notch at 1735 MPa, as show in Fig. 4(c) (Stage II). In stage III, a stable plastic deformation arises, resulting in lots of shear bands formation and propagation, as shown in Fig. 4(d). Then, the main shear band is formed when the stress increases and the sample is finally separated in stage IV [Fig. 4(e)].

Similarly to the Zr-based MG, four distinct deformation evolution stages are also recognized in the Ce-based MG. In stage I, the sample manifests the elastic deformation without any shear bands below 102 MPa [Fig. 4(f)], and there are no shear bands but a crack emerges at 102 MPa in stage II [Fig. 4(g)]. In stage III, the stress lies between 102 and 196 MPa and the crack propagates steadily [Fig. 4(h)]. In stage IV, the crack propagates catastrophically and inevitably results in the final fracture of the sample.

Different from above two MGs, only two stages for the Mg-based MG
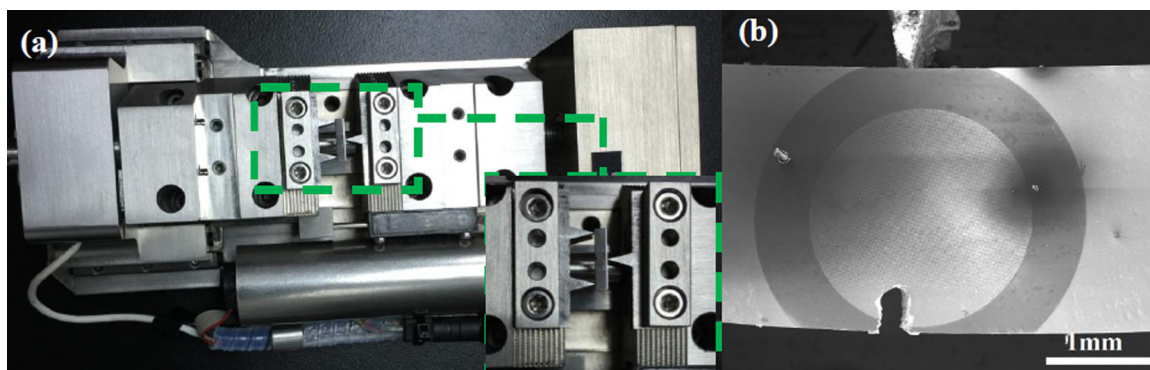
Fig. 1. Experimental setup. (a) Detail of the miniature three-point bending test frame with a specimen mounted. (b) Three-point bending sample under loading in SEM chamber.
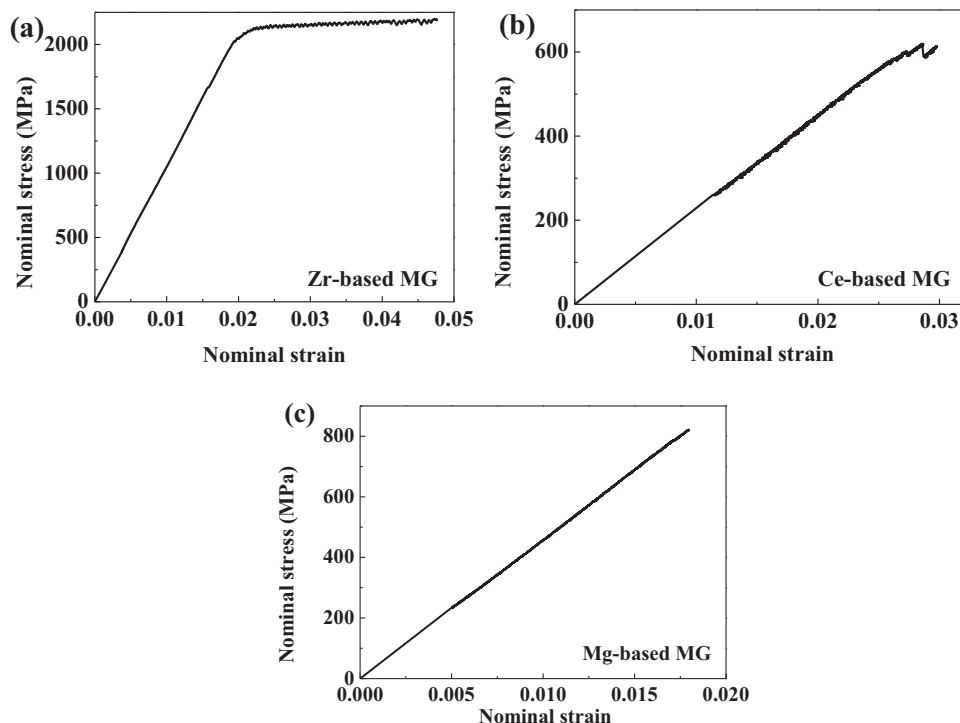
Fig. 2. Normal compression stress-strain curves of the three MGs.
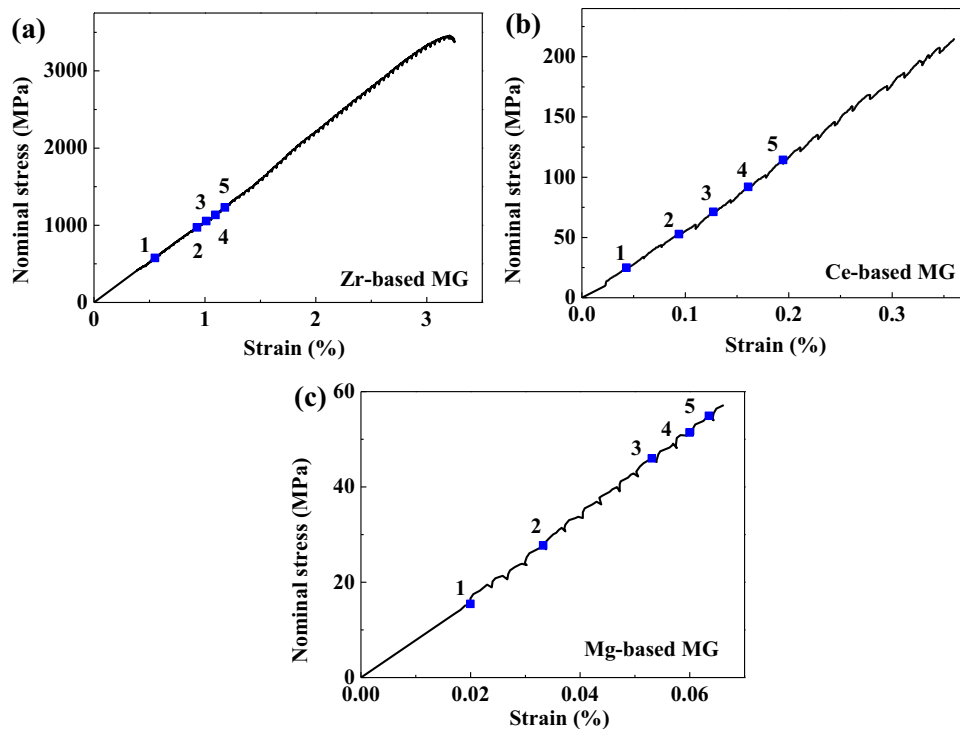
Fig. 3. Normal stress-midpoint strain curves of three MGs under three-point bending test.

are observed. In the first stage, the corresponding load is less than 54 MPa and the Mg-based MG undergoes an elastic deformation. In the second stage, the corresponding load reaches 56 MPa and a catastrophic failure occurs without any shear bands.

The fracture surfaces of the MGs after bending are shown in Fig. 5. For the Zr-based MG, the whole profile of facture surface shows rough ridge and valley patterns [Fig. 5(a)]. The radial vein patterns with some molten droplets are displayed on the fracture surface of the Zr-based MG [Fig. 5(b)], which indicates highly localized plastic softening. For the Ce-based MG, the "rough zone" appears only at the crack initiation place [Fig. 5(c)]. With the crack propagating, the roughness becomes minimal. Unlike the case of the Zr-based MG, there is a large density of dimples without significantly melting droplets on the fracture surface in the Ce-based MG [Fig. 5(d)], which suggests that no serious plastic softening occurs during bending fracture. For the Mg-based MG, no obviously rough zone on the fracture surface [Fig. 5(e)], and a large
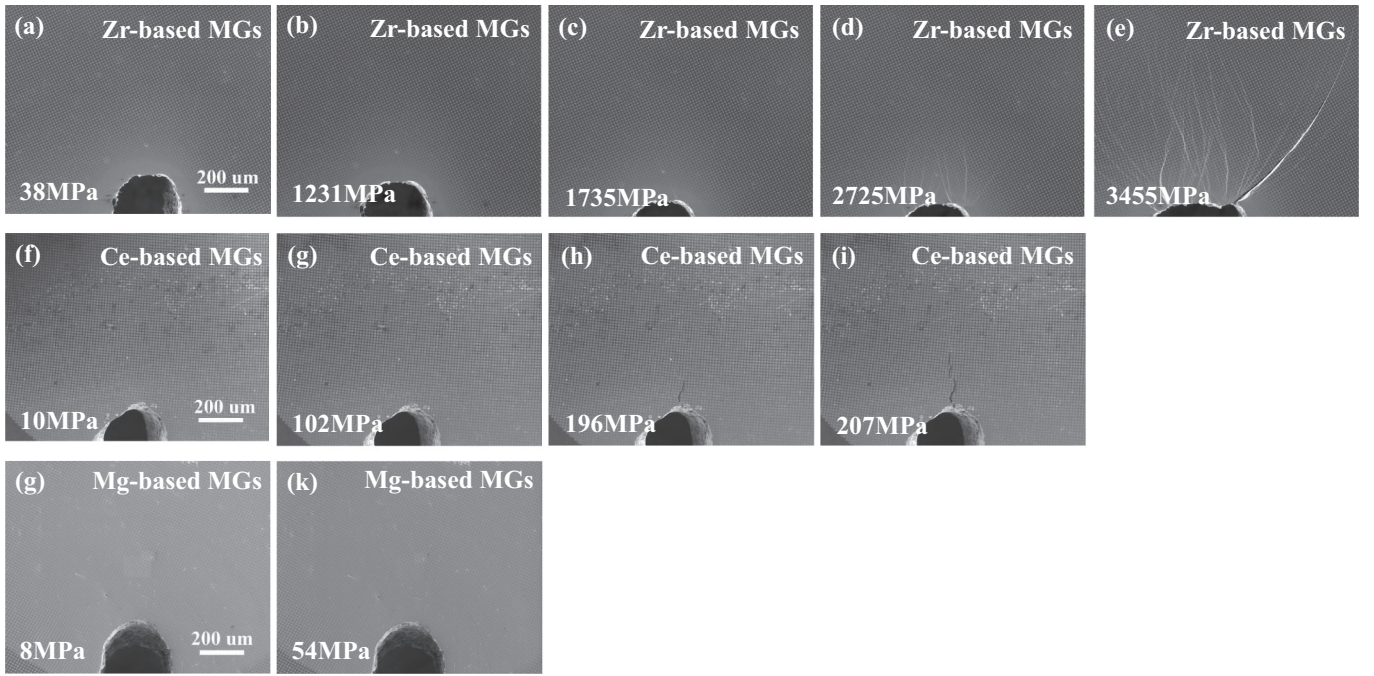
Fig. 4. Side-view SEM images of three MGs during three-point bending test. (a–e) The Zr-based MG at normal stresses of 38, 1231, 1735, 2725 and 3455 MPa, respectively. (f–i) The Ce-based MG at normal stresses of 10, 125, 196 and 207 MPa, respectively. (g–k) The Mg-based MG at normal stresses of 8 and 54 MPa, respectively.

amount of nano-scale periodic patterns, such as dimples and stripes appear in nano-scale [Fig. 5(f)].

To further investigate the failure mode of the MGs, the DIC method is adopted here to explore the strain field distribution. Figs. 6(a), 7(a) and 8(a) display the uniform mesh-pattern images in three unloaded MGs. The normal strain (perpendicular to the crack plane) map of ε_x, the ε_y fields along the loading direction (y-axis) and the shear-strain (γ_{xy}) fields can be calculated with the reference image without load. The maximum linear strain in x-axis (ε_{xmax}) and y-axis (ε_{ymax}), and the maximum shear strain, γ_{max}, are deduced by the following equation [32],

$$\begin{cases} \varepsilon_{xmax} = \frac{1}{2}\left[\varepsilon_x + \varepsilon_y - \sqrt{(\varepsilon_x - \varepsilon_y)^2 + \gamma_{xy}^2}\right] \\ \varepsilon_{ymax} = \frac{1}{2}\left[\varepsilon_x + \varepsilon_y + \sqrt{(\varepsilon_x - \varepsilon_y)^2 + \gamma_{xy}^2}\right] \\ \gamma_{max} = \sqrt{(\varepsilon_x - \varepsilon_y)^2 + \gamma_{xy}^2} \end{cases}$$

(3)

Fig. 6(b)–(d) show a series of ε_{xmax}, ε_{ymax} and γ_{max} fields of the Zr-based MG at different stresses indicated by the numbers in Fig. 3(a), respectively. In the ε_{ymax} and γ_{max} fields, some high strain-concentration striations emerge at 577 MPa. Subsequently, the strain-concentration striations evolve from two to four when the stress increases from 577 to 1231 MPa. In contrast to the SEM image in Fig. 4(b), there is no significant shear band and the sample still remains in the elastic regime at 1231 MPa. Unlike the ε_{ymax} and γ_{max} fields, the strain-concentration in the ε_{ymax} field is isolated.

The different fracture modes of three model MGs under three-point bending can be analyzed by the free-volume theory. The strain distributions of the Zr-based MG show some separated strain-concentration striations before yielding (Fig. 6). The multiple high strain-concentration striations are helpful to disperse the strain into different strain-concentrated regions, and shear softening occurs simultaneously. More strain-concentrated regions can alleviate the stress concentration, which prevent from cracking and breaking. As SEM imagine of Fig. 4(b), no obvious shear band occurs below 1735 MPa. Previous studies have found that the regions with numerous free volumes are able to facilitate initially nucleating and branching of shear bands [27,29]. In the present study, some locally plastic deformation after the elastic stage, and some shear bands emerge around the notch in the Zr-based MG [Fig. 4(c)]. Subsequently, in the separated strain-concentrated striations, multiple shear bands occur and propagate steadily after yielding [Fig. 4(d)]. With increasing the load, the main shear band emerges eventually from the multiply shear bands [Fig. 4(e)]. Then, the main shear band will further propagate and provide the midpoint displacement or strain until the failure of the Zr-based MG occurs. Thus, the strain-concentrated regions act as the original place for shear banding in ductile MGs, or cracking in brittle MGs. In this case, it can be rationally assumed that numerous free volumes are activated in the strain-concentrated regions that can be treated as soft regions. The regions without strain concentrations behave as the hard regions that is speculated to contain a small number of free volumes. These hard regions are beneficial for impeding the rapid propagation of shear bands.

Fig. 7 shows the evolution of strains for the Ce-based MG. With increasing the stress, the phenomenon of strain concentration becomes more prominent [Fig. 7(b) and (d)]. The strain-concentration striations are obviously found to be formed in the ε_{xmax} and γ_{max} fields but seldom appear in the ε_{ymax} field. Unlike the Zr-based MG, the three strain-concentration striations of the Ce-based MG are located around the notch. Responding to the continued loading, the stress in the strain-concentrated regions gradually increases. When the stress firstly reaches the yield stress, σ_y, the initial main shear band emerges in the middle of the notch because the strain-concentration striations concentrate here, shown in Fig. 4(h). Then, a shear displacement occurs, which causes the stress at the tip of the main shear band decreases to σ_1 ($< \sigma_y$), due to locally shear-softening and stress gradient under three-point bending. Thus, the main shear band stops propagating [29]. With continued loading, the competition occurs between activating new shear bands and forming cavities. A dimensionless parameter, f, is formulated as the activation barriers for shear flow or cavitation to describe the crack initiation in a shear band [33],
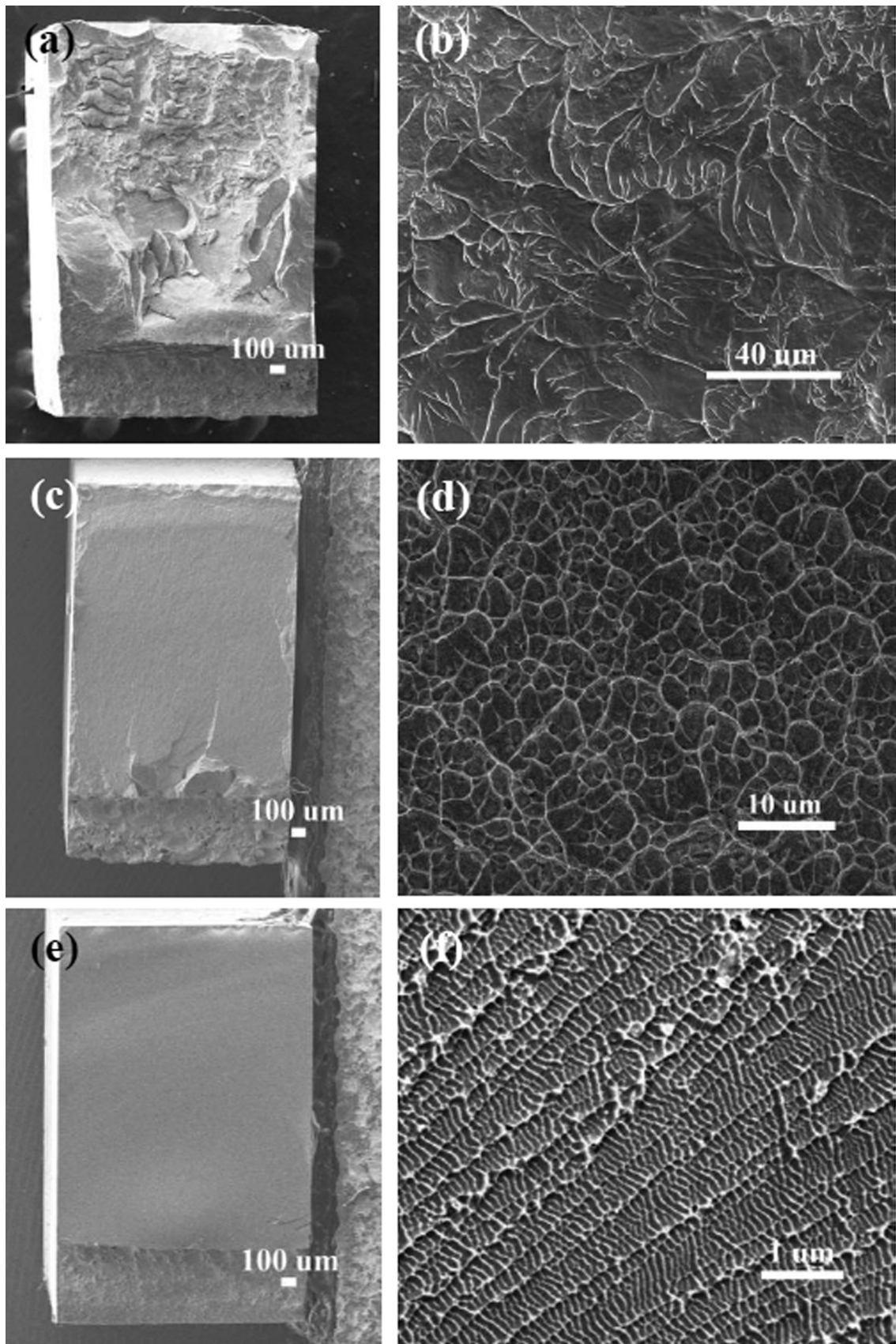
Fig. 5. Fractographies of the three MGs. (a) Overview of Zr-based MG. (b) Crack propagation zone of Zr-based MG. (c) Overview of Ce-based MG. (d) Crack propagation zone of Ce-based MG. (e) Overview of Mg-based MG. (f) Crack propagation zone of Mg-based MG.
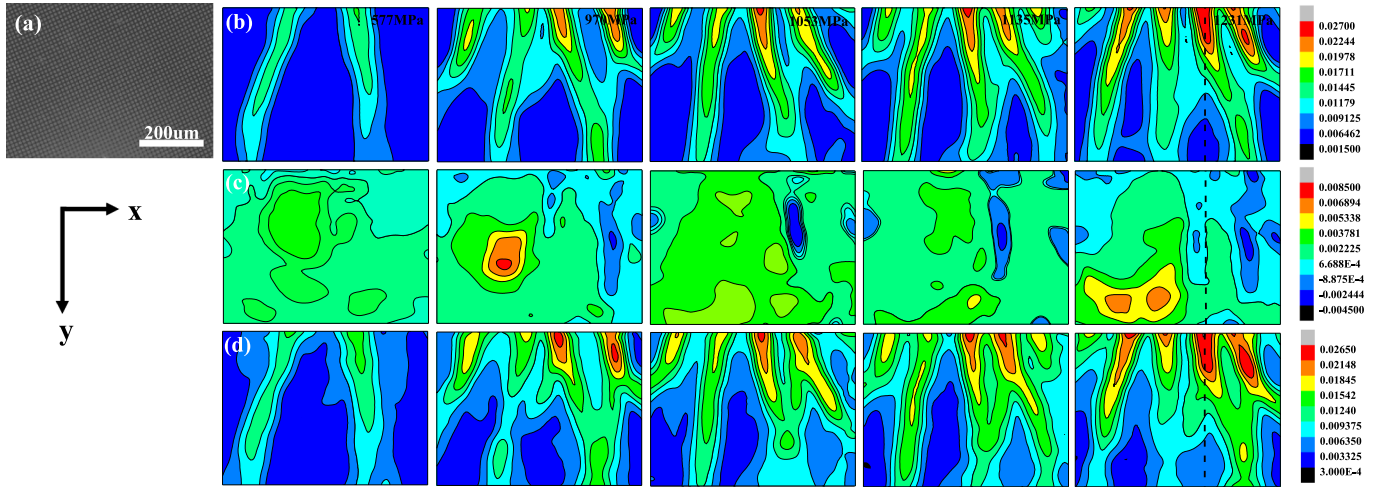
Fig. 6. DIC images of Zr-based MG in the elastic regime under load. (a) Uniform mesh-pattern images of unloaded Zr-based MG, (b), (c) and (d) are the ε_{xmax} field, ε_{ymax} field and γ_{max} field obtained from DIC, respectively.

$$log(f) \sim \frac{T_g}{T}\left(\frac{B}{G}-1\right), \tag{4}$$

where T_g and T are the glass-transition and reference temperatures, B and G are the bulk and shear moduli, respectively. Therefore, the capacity for shear flow before cavitation of material can be explored from the glass-transition temperature and elastic constants. For the Ce-based MG, the value of $log (f)$ is less than half of that in the Zr-based MG (Table 1), implying that the Ce-based MG tends to form cavities to deform. Additionally, it can be observed that the interface length between the concentrated and un-concentrated regions of the Ce-based MG is less than that of Zr-based MG, which may indicate that the impediment effect on the interface of the Ce-based MG is weaker than that in the Zr-based MG. As a result, the initiation of new secondary shear bands around the main shear band is more difficult than the formation of cavitation in the formed shear band. Thus, there is no obviously shear-band branching before cracking, as shown in Fig. 4(h) and (i).

When the load is more than 115 MPa, the critical crack length is reached, and then the unstable fracture occurs, producing two broken parts.

Fig. 8 exhibits the strain fields from DIC results of the Mg-based MG. The strain-concentration striations of $\varepsilon_{x max}$, $\varepsilon_{y max}$ and γ_{max} all emerge at the beginning of loading [Fig. 8(b)–(d)]. However, with increasing load, they begin to disappear and the corresponding isolated strain-concentration regions gradually form, especially in the ε_{xmax} and γ_{max} fields [Fig. 8(b) and (d)]. Among these three MGs, the Mg-based MG is verified to be the only one that strain-concentration striations are localized in a few isolated regions (Fig. 8). Two points can be addressed to explain the fracture process of Mg-based MG. Firstly, with increasing the load, the elastic energy is absorbed in the strain-concentration regions, which causes an expansion tendency of the isolated strain-concentration region. The value of $log (f)$ for the Mg-based MG is less than that of the Ce-based MG (Table 1). When an initial fracture emerges, the cavitation occurs in the Mg-based MG, and then leads to fracture.
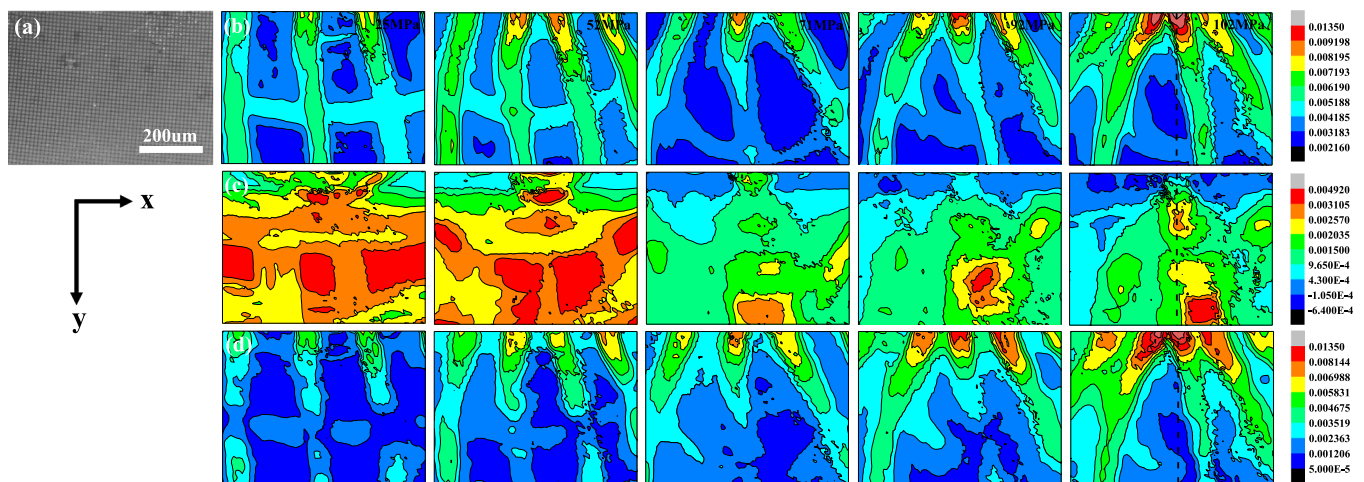
Fig. 7. DIC images of Ce-based MG in the elastic regime under load. (a) Uniform mesh-pattern images of unloaded Ce-based MG. (b), (c) and (d) are the ε_{xmax} field, ε_{ymax} field and γ_{max} field obtained from DIC, respectively.
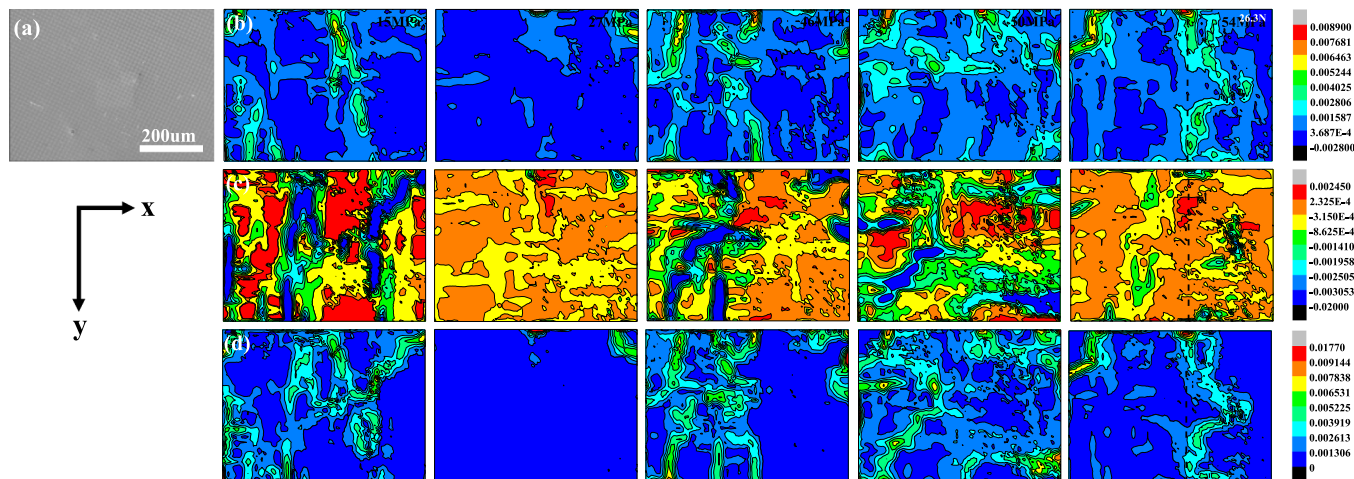
Fig. 8. DIC images of Mg-based MG in the elastic regime under load. (a) Uniform mesh-pattern images of unloaded Mg-based MG. (b), (c) and (d) are the ε_{xmax} field, ε_{ymax} field and γ_{max} field obtained from DIC, respectively.
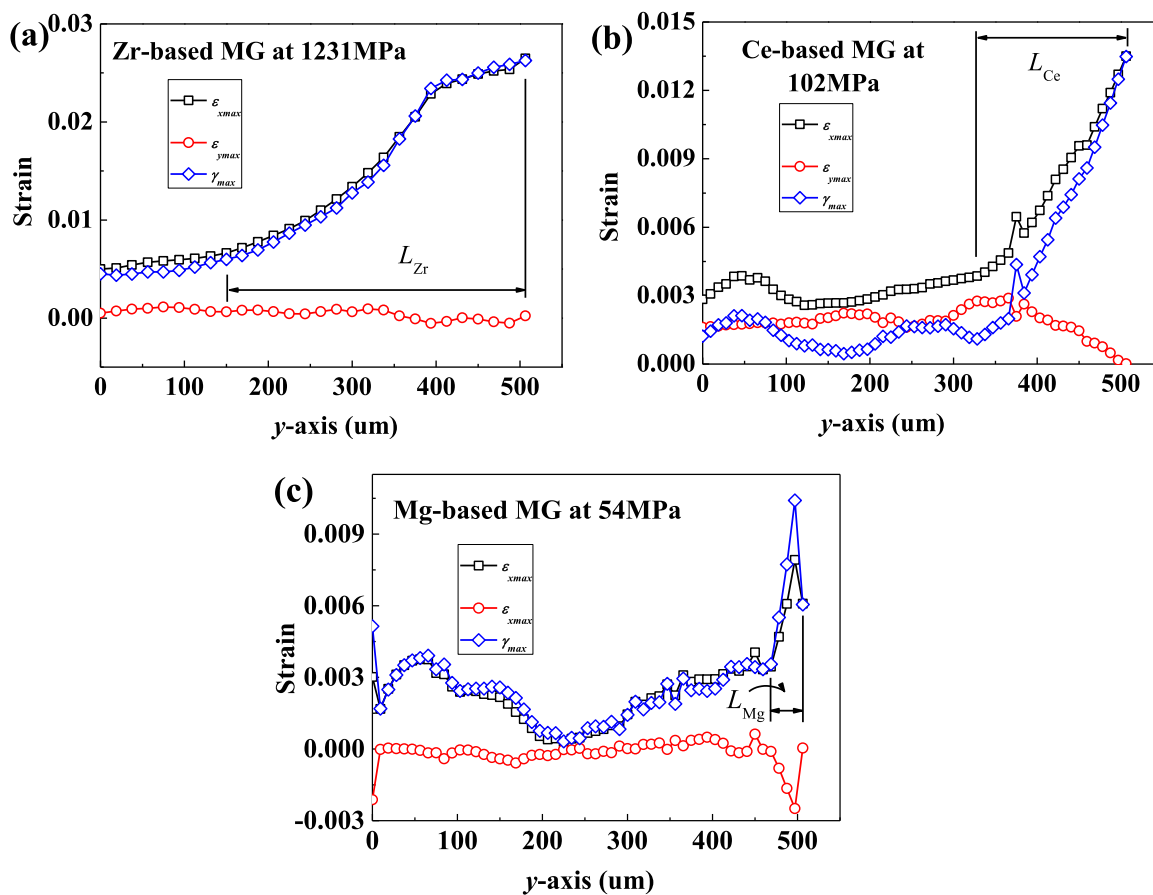
Fig. 9. Profile of the distributions of the ε_{xmax}, ε_{ymax} and γ_{max} values at the maximum stress of three MGs in the elastic regime on the maximum shear stress plane, *i.e.,* along the dash lines in Figs. 4–6. (a–c) The distributions of the ε_{xmax}, ε_{ymax} and γ_{max} values of the Zr-based MG at 1231 MPa, the Ce-based MG at 102 MPa, and the Mg-based MG at 54 MPa, respectively.

Secondly, the average radius of the first coordination unit of covalent bonding is found to be about 0.25 nm [34]. The bonding lengths of Mg-Mg and Mg-Cu atomic pairs are 0.272 nm and 0.253 nm, respectively [34], which are close to the covalent bonding distances. Therefore, a large fraction of covalent bonds is another reason for the cleavage

fracture mode [7]. In this case, the Mg-based MG is concluded to be more sensitive to fracture in a cleavage mode than the Ce-based MG. Moreover, when the stress is more than 56 MPa, there is no obvious shear band but crack propagates at an unstable level.

Finally, to further examine the fracture feature, the distributions of

ε_{xmax}, ε_{ymax} and γ_{max} values for the Zr-, Ce- and Mg-based MGs on the maximum shear-stress plane (along the dash lines in Figs. 6–8) before yielding are demonstrated in Fig. 9. It can be observed that for the Zr- and Ce-based MGs, both of ε_{xmax}, and γ_{max} values rise with increasing the value of y along the crack propagation direction [Fig. 9(a) and (b)]. They reach the maximum values eventually nearby the notch of the Zr- and Ce-based MGs. Due to the existence of a much small ε_{ymax} value in three-point bending condition, the ε_{xmax} and γ_{max} curves overlap approximately with each other [Fig. 9(a)]. For the Zr-based MG, the length, L_{Zr}, of the strain-concentration region is measured to be about 356 μm at 1231 MPa. In Fig. 9(b), the distribution profiles of the ε_{xmax}, ε_{ymax} and γ_{max} values at 102 MPa are mapped. The value of L_{Ce} is approximately 178 μm [Fig. 9(b)], which is almost 50% smaller than the value in the Zr-based MG. As shown in Fig. 9(c), the value of L_{Mg} is observed to be approximately 38 μm, which is the minimum value among the three MGs.

4. Conclusion

Through the integrated method of the *in-situ* electron microscopy mechanical testing technique and the digital image correlation technique, the impact of free volume on shear band multiplication and bending plasticity of MGs is studied. The following conclusions can be drawn:

(1) The strain-concentration striations before yielding are examined to be significant beneficial to the subsequent shear band multiplication. Thus, it can be reasonably speculated that, during the strain evolving to be concentrated, numerous free volumes are activated in the strain-concentrated regions. After yielding, these strain-concentration striations can be treated as soft regions in which shear banding occurs. The multiple high strain-concentration striations can disperse the strain into different regions, and absorb lots of elastic energy. While the un-concentrated regions is assumed to contain a small number of free volumes, which can impede the rapid propagation of shear bands. This inhomogeneous distribution of the strain-concentrated regions behave the work softening and hardening effects, which can further improve shear band multiplication.

(2) The shear band multiplication has a significant effect on bending plasticity of MGs. The competition between activating new shear bands and forming cavities dominates the fracture mode and bending plasticity when the initial shear band emerges. For the Zr-based MG, the multiple shear bands frequently occur after yielding, which could improve its bending plasticity. For the Ce-based MG, due to cavitation in the initial shear band, there is no obvious shear band but initial crack when yielding. Different from the cases in the Zr- and Ce-based MGs, the cavitation dominates the fracture process of the Mg-based MG.

(3) The number and the length of strain-concentration striations with a large number of free volumes before yielding are verified to play import roles in bending plasticity of MGs. Among the Zr-, Ce- and Mg-based MGs, the Zr-based MG with the maximum and longest striations presents the best macroscopic bending plasticity, while Mg-based MG with separated and smallest strain-concentration regions exhibits no obvious plastic deformation.

Acknowledgements

References

[1] W.L. Johnson, Bulk glass-forming metallic alloys: science and technology, MRS Bull. 24 (1999) 42–56.
[2] W.H. Wang, The elastic properties, elastic models and elastic perspectives of metallic glasses, Prog. Mater. Sci. 57 (2012) 487–656.
[3] P.P. Wang, J.Q. Wang, H. Li, H. Yang, J.T. Huo, J.G. Wang, C.T. Chang, X.M. Wang, R.W. Li, G. Wang, Fast decolorization of azo dyes in both alkaline and acidic solutions by Al-based metallic glasses, J. Alloy Compd. 701 (2017) 759–767.
[4] M.F. Ashby, A.L. Greer, Metallic glasses as structural materials, Scr. Mater. 54 (2006) 321–326.
[5] A. Lenain, J.J. landin, G. Kapelski, F. Volpi, S. Gravier, Hf-rich bulk metallic glasses as potential insulating structural material, Mater. Des. 139 (2018) 467–472.
[6] F. Spaepen, A microscopic mechanism of steady state inhomogeneous flow in metallic glasses, Acta Metall. 25 (1977) 407–415.
[7] S.H. Chen, K.C. Chan, L. Xia, Effect of stress gradient on the deformation behavior of a bulk metallic glass under uniaxial tension, Mater. Sci. Eng. A 574 (2013) 262–265.
[8] F. Jiang, Y.L. Zhao, L.C. Zhang, S.B. Pan, Y.G. Zhou, L. He, J. Sun, Dependence of ductility on free volume in a Cu-Zr based metallic glass, Adv. Eng. Mater. 11 (2009) 177–181.
[9] W.D. Li, Y.F. Gao, H.B. Bei, On the correlation between microscopic structural heterogeneity and embrittlement behavior in metallic glasses, Sci. Rep. 5 (2015) 14786.
[10] R. Rashidi, M. Malekan, R. Gholamipour, Microstructure and mechanical properties of a Cu-Zr based bulk metallic glass containing atomic scale chemical heterogeneities, Mater. Sci. Eng. A 729 (2018) 433–438.
[11] B.A. Sun, W.H. Wang, The fracture of bulk metallic glasses, Prog. Mater. Sci. 74 (2015) 211–307.
[12] Z.F. Zhang, J. Eckert, L. Schultz, Difference in compressive and tensile fracture mechanisms of $Zr_{59}Cu_{20}Al_{10}Ni_8Ti_3$ bulk metallic glass, Acta Mater. 51 (2003) 1167–1179.
[13] G. Wang, K.C. Chan, X.H. Xu, W.H. Wang, Instability of crack propagation in brittle bulk metallic glass, Acta Mater. 56 (2008) 5845–5860.
[14] L.L. Zhang, R. Li, T. Xu, H.Y. Zhang, T. Zhang, Ternary La-Al-C bulk metallic glasses, Intermetallics 52 (2014) 92–96.
[15] C.C. Tasan, J.P.M. Hoefnagels, M. Diehl, D. Yan, F. Roters, D. Raabe, Strain localization and damage in dual phase steels investigated by coupled *in-situ* deformation experiments and crystal plasticity simulations, Int. J. Plast. 63 (2014) 198–210.
[16] Y.P. Lu, X.Z. Gao, L. Jiang, Z.N. Chen, T.M. Wang, J.C. Jie, H.J. Kang, Y.B. Zhang, S. Guo, H.H. Ruan, Y.H. Zhao, Z.Q. Cao, T.J. Li, Directly cast bulk eutectic and near-eutectic high entropy alloys with balanced strength and ductility in a wide temperature range, Acta Mater. 124 (2017) 143–150.
[17] B. Pan, Recent progress in digital image correlation, Exp. Mech. 51 (2011) 1223–1235.
[18] B. Pan, Digital image correlation for surface deformation measurement: historical developments, recent advances and future goals, Meas. Sci. Technol. 29 (2018) 082001.
[19] A.M. Korsunsky, T. Sui, E. Salvati, E.P. George, M. Sebastiani, Experimental and modeling characterization of residual stresses in cylindrical samples of rapidly cooled bulk metallic glass, Mater. Des. 104 (2016) 235–241.
[20] R.H. Zhu, H.M. Xie, Y.F. Xue, L. Wang, Y.J. Li, Fabrication of speckle patterns by focused ion beam deposition and its application to microscale residual stress measurement, Meas. Sci. Technol. 26 (2015) 095601.
[21] B. Winiarski, P.J. Withers, Novel implementations of relaxation methods for measuring residual stresses at the micron, J. Strain Anal. 50 (2015) 412–425.
[22] B. Winiarski, R.M. Langford, J.W. Tian, Y. Yokoyama, P.K. Liaw, P.J. Withers, Mapping residual stress distributions at the micron scale in amorphous materials, Metall. Mater. Trans. A 41A (2010) 1743–1751.
[23] S.H. Joo, H. Kato, K. Gangwar, S. Lee, H.S. Kim, Shear banding behavior and fracture mechanisms of $Zr_{55}Al_{10}Ni_5Cu_{30}$ bulk metallic glass in uniaxial compression analysed using a digital image correlation method, Intermetallics 32 (2013) 21–29.
[24] J. Zhang, P. Aimedieu, F. Hild, S. Roux, T. Zhang, Complexity of shear localization in a Zr-based bulk metallic glass, Scr. Mater. 61 (2009) 1145–1148.
[25] Y. Wu, H. Bei, Y.L. Wang, Z.P. Lu, E.P. George, Y.F. Gao, Deformation-induced spatio-temporal fluctuation, evolution and localization of strain fields in a bulk metallic glass, Int. J. Plast. 71 (2015) 136–145.
[26] J. Li, Y.W. Wang, J. Yi, I. Hussain, R. Li, B. Zhang, G. Wang, Strain-energy transport during fracture of metallic glasses, J. Alloy Compd. 680 (2016) 43–53.
[27] Y. Hu, H.H. Yan, J.F. Li, Y.H. Zhou, Bending plasticity of $Zr_{55}Al_{10}Ni_5Cu_{30}$ bulk metallic glass with monolithic amorphous structure, J. Alloy Compd. 688 (2016) 620–625.
[28] G.N. Yan, Y. Shao, K.F. Yao, A non-viscous-featured fractograph in metallic glasses, Philos. Mag. 96 (2016) 542–550.
[29] L.C. Zhang, F. Jiang, Y.L. Zhao, S.B. Pan, L. He, J. Sun, Shear band multiplication aided by free volume under three-point bending, J. Mater. Res. 25 (2010) 283–291.
[30] Y.J. Huang, Z.L. Ning, Z. Shen, W.Z. Liang, H.C. Sun, J.F. Sun, Bending behavior of as-cast and annealed ZrCuNiAl bulk metallic glass, J. Mater. Sci. Technol. 33 (2017) 1153–1158.
[31] Y. Zhang, J.P. Liu, S.Y. Chen, X. Xie, P.K. Liaw, K.A. Dahmen, J.W. Qiao, Y.L. Wang, Serration and noise behaviors in materials, Prog. Mater. Sci. 90 (2017) 358–460.
[32] R.J. Atkin, N. Fox, An Introduction to the Theory of Elasticity, Longman, 1980.
[33] M.D. Demetriou, M.E. Launey, G. Garrett, J.P. Schramm, D.C. Hofmann, W.L. Johnson, R.O. Ritchie, A damage-tolerant glass, Nat. Mater. 10 (2011) 123–128.
[34] J.J. Pan, M.J. Tan, K.M. Liew, On valence electron density, energy dissipation and plasticity of bulk metallic glasses, J. Alloy Compd. 577S (2013) S56–S65.
[35] W.H. Wang, R.J. Wang, G.J. Fan, J. Eckert, Formation and properties of Zr-(Ti, Nb)-Cu-Ni-Al bulk metallic glasses, Mater. Trans. 42 (2001) 587–591.
[36] B. Zhang, D.Q. Zhao, M.X. Pan, R.J. Wang, W.H. Wang, Formation of cerium-based bulk metallic glasses, Acta Mater. 54 (2006) 3025–3032.
[37] X.K. Xi, R.J. Wang, D.Q. Zhao, M.X. Pan, W.H. Wang, Glass-forming Mg-Cu-Re (Re = Gd, Pr, Nd, Tb, Y, and Dy) alloys with strong oxygen resistance in manufacturability, J. Non-Cryst. S. 344 (2004) 105–109.